ACS Photonics

Article

pubs.acs.org/journal/apchd5

Dielectric Resonator Reflectarray as High-Efficiency Nonuniform Terahertz Metasurface

Daniel Headland,[*,†] Eduardo Carrasco,[‡,¶] Shruti Nirantar,[§,∥] Withawat Withayachumnankul,[†,⊥] Philipp Gutruf,[§,∥] James Schwarz,[§,∥] Derek Abbott,[†] Madhu Bhaskaran,[§,∥] Sharath Sriram,[§,∥] Julien Perruisseau-Carrier,[‡] and Christophe Fumeaux[†]

[†]School of Electrical and Electronic Engineering, The University of Adelaide, Adelaide, SA 5005, Australia

[‡]École Polytechnique Fédérale de Lausanne, EPFL, 1015 Lausanne, Switzerland

[¶]Foundation for Research on Information Technologies in Society, IT'IS, 8004 Zürich, Switzerland

[§]Functional Materials and Microsystems Research Group and [∥]MicroNano Research Facility, RMIT University, Melbourne, Victoria 3000, Australia

[⊥]Interdisciplinary Graduate School of Science and Engineering, Tokyo Institute of Technology, Ookayama, Meguro-ku, Tokyo 152-8550, Japan

ABSTRACT: Advances in terahertz technology rely on the combination of novel materials and designs. As new devices are demonstrated to address the terahertz gap, the ability to perform high-efficiency beam control will be integral to making terahertz radiation a practical technology. Here, we use a metasurface composed of nonuniform dielectric resonator antennas on a ground plane to achieve efficient beam focusing at 1 THz. The dielectric resonators are made of high-resistivity silicon, which is a low-loss, nondispersive material for terahertz waves. The resonators operate around the resonance of the displacement current in the silicon, which is crucial to attaining high efficiency. The reflectarray's capacity to focus terahertz radiation is experimentally verified, and hence by the principle of antenna reciprocity, it can also be employed as a terahertz collimator. The demonstrated device can therefore be deployed for high-gain terahertz antennas. Further measurements show that the loss of the reflectarray is negligible, which confirms the high efficiency of the dielectric resonators. This finding will enable the design of efficient flat-profile terahertz reflectarrays and metasurfaces to serve arbitrary beam control requirements in the near and far fields.

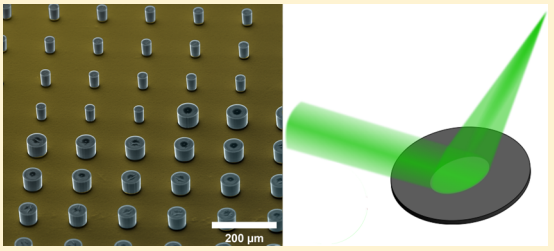

KEYWORDS: *dielectric resonator antenna (DRA), metasurfaces, reflectarrays, terahertz technology, flat optics, focusing mirror*

The terahertz spectral range has significant potential for applications including communications,[1,2] noninvasive medical imaging,[3,4] security screening,[5] and pharmaceutical quality control.[6,7] However, absorption of terahertz radiation is strong in typical atmospheric conditions, and hence directional or high-gain antennas are required in order to maintain adequate signal strength over a realistic propagation distance.[1,2,8−11] Passive devices that shape the wavefront of electromagnetic radiation offer a way of achieving high-gain antennas that can be coupled to arbitrary field sources. This has traditionally been achieved with either bulky lenses made of terahertz-transparent materials,[12−15] or physically shaped mirrors. Thinner and flat-profile devices are preferable for compact systems. Such devices are typically implemented with nonuniform arrays of subwavelength elements that each impart some local alteration on reflected or transmitted fields. Importantly, these devices also offer greater control and freedom over the resultant beam profile, while being highly suited to large-scale fabrication. One example of such a device is a reflectarray, which can be considered a flat-profile beam-shaping reflector antenna.[16] In general, reflectarray antennas have moderate loss, low cross-polarization, and the potential for reconfigurability and dynamic control.[17,18]

In the terahertz range, reflectarray antennas are most commonly implemented using metallic resonators.[19−22] Resonators of this type typically exhibit magnetic dipole modes of resonance, and the resonance frequency can be tuned by adjusting physical resonator dimensions. On-resonance, both incident and reflected electric fields are in-phase, and hence the resonator exhibits a 0° reflection phase. When operated off-resonance, the reflection phase gradually deviates from 0°. Therefore, the reflection phase can be controlled with careful selection of resonator dimensions. Thus, a series of resonators with different sizes can cover a range of phase discontinuities of close to 360°, which is sufficient to construct a 2D phase profile for an arbitrary beam control application. In addition to supporting applications requiring phase control, metallic resonators are important devices in the terahertz range and have made significant contributions to the development of

Received: February 13, 2016
Published: May 13, 2016

DOI: 10.1021/acsphotonics.6b00102
ACS Photonics 2016, 3, 1019−1026

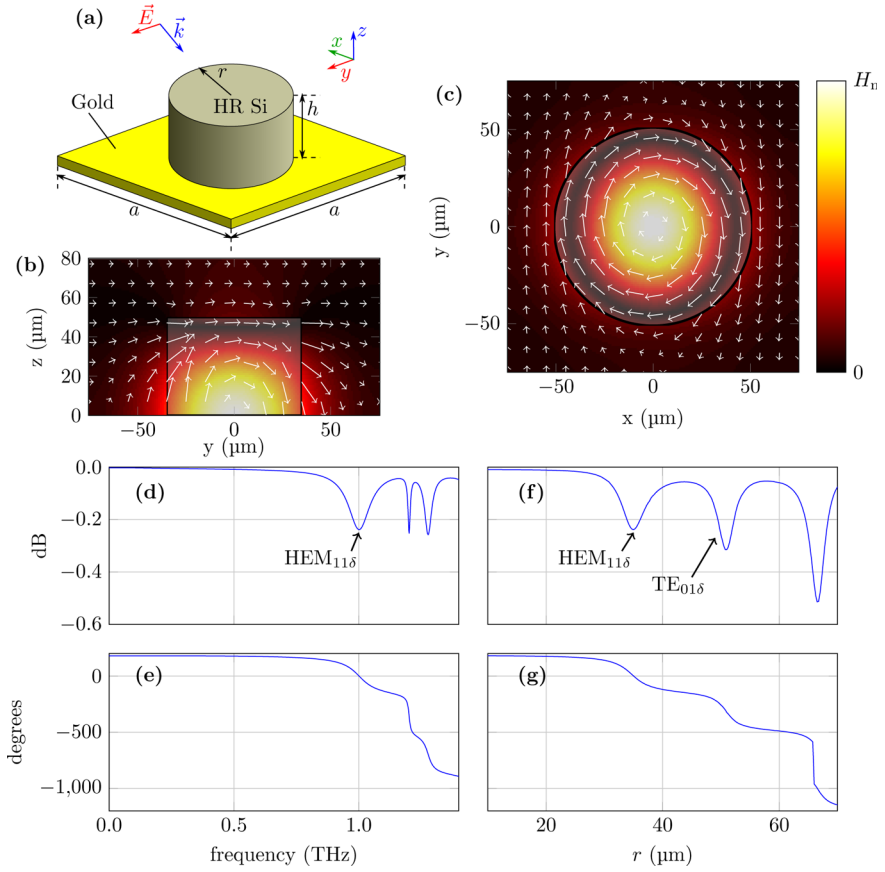

Figure 1. Design and simulated elecromagnetic response of the dielectric resonator antenna unit cell. (a) Resonator structure, where h = 50 μm and a = 150 μm, and incident TE excitation is at a 45° angle of incidence, (b) HEM$_{11\delta}$ mode of resonance at 1 THz, when r = 35 μm, with magnetic field strength shown as a heat map and electric field shown as a quiver plot, viewed from the side, (c) TE$_{01\delta}$ mode of resonance at 1 THz, when r = 51 μm, viewed from above, at a distance of 34 μm away from the ground plane, (d, e) broadband amplitude and phase responses when r = 35 μm, showing fundamental resonance at 1 THz, and (f, g) amplitude and phase responses for parametric sweep of cylinder radius, at an operating frequency of 1 THz.

terahertz technology. As such, metallic resonators have been employed for numerous terahertz devices including waveplates,[23,24] active devices,[25,26] and sensing devices.[27,28] However, terahertz devices based on metallic resonators typically suffer from significant conductor and dielectric losses.[29,30]

A high-efficiency alternative to metallic resonators is the dielectric resonator antenna (DRA), which operates based on the resonance of the displacement current in dielectric structures of moderate to high refractive index. At a phenomenological level, this is due to internal reflection at the dielectric−air boundary, which confines electromagnetic radiation into standing waves at certain frequencies. Given that conduction losses in a metallic structure increase with frequency, the DRA was originally developed as a means of minimizing on-resonance conduction current for efficient operation at high frequencies.[31] As a result, DRAs are well suited to microwave frequencies[32,33] and millimeter waves[34−36] and have been demonstrated in the submillimeter[37,38] and optical ranges.[39,40]

In the past, DRAs in array configurations have been employed for beam-forming applications in the microwave[41] and optical ranges.[42,43] At terahertz frequencies, however, DRA-based reflectarrays have been relatively unexplored, as the fabrication of such structures is challenging and requires the development of unconventional processes. Recently, we have demonstrated a homogeneous array of highly efficient, single-crystal silicon DRAs for an artificial magnetic conductor application.[44] These DRAs exhibited a full range of reflection phase response around the fundamental resonance frequency and had higher order resonances that further extend the phase tunability range, making them appealing for beam-shaping applications. In this work, a terahertz reflectarray composed of DRAs, with the functionality of an off-axis focusing mirror operating at 1 THz, is realized and experimentally demonstrated.

RESULTS AND DISCUSSION

DRA Resonance Modes. Each DRA is made up of a microscale cylinder of high-resistivity single-crystal float-zone silicon (HR Si) on a gold ground plane, as shown in Figure 1a. Intrinsic silicon of this form is chosen due to its extremely low loss in the terahertz range (tan $\delta < 4 \times 10^{-5}$) and its moderate relative permittivity (ϵ_r = 11.68), which make it appropriate for a dielectric resonator intended to couple to free-space fields.[31] Excitation is provided by a TE-polarized plane wave with a 45° angle of incidence. The lattice constant of the array is a = 150 μm, which corresponds to half a wavelength at the operating frequency of 1 THz. This is chosen to be subwavelength in order to suppress grating lobes, including when oblique incidence is accounted for. The response and modes of resonance of the DRA are investigated with full-wave simulations, for 45° incidence and TE polarization. In

DOI: 10.1021/acsphotonics.6b00102
ACS Photonics 2016, 3, 1019−1026

simulation, the array is treated as homogeneous and of infinite extent in both in-plane dimensions.

When set to have a radius of r = 35 μm and height of h = 50 μm, the DRA exhibits a fundamental resonance at 1 THz. This takes the form of a horizontal magnetic dipole on a ground plane, or $HEM_{11\delta}$ mode, as shown in Figure 1b. When the radius is set to r = 51 μm, the DRA exhibits a higher order resonance at 1 THz, and the field distribution inside the DRA is a vertically oriented magnetic dipole, or $TE_{01\delta}$ mode,[45] as shown in Figure 1c. The magnetic dipole orientation results in electric fields that are parallel to the ground plane. Given that the tangential electric field vanishes at the surface of a good conductor, the fields are strongest a distance away from the metal. For this reason, the field plot shown in Figure 1c is at a distance of 34 μm from the ground plane.

The r = 35 μm configuration, which exhibits fundamental resonance at 1 THz, is investigated in more detail, and a broadband response is given in Figure 1d,e. This shows the expected 0° reflection phase on the fundamental resonance, as well as higher order resonances beyond 1.2 THz. The multiple resonances jointly form a large phase transition, with dissipation loss that does not exceed 0.25 dB.

The fundamental resonance frequency is tunable by varying the radius of the microscale cylinder. Thus, parametric analysis at 1 THz is performed in order to determine the phase tunability of the DRA structure with respect to the cylinder radius r. The parametric sweep results given in Figure 1f,g show resonances at radius values of r = 35, 51, and 67 μm. Given that the first two resonances form a smooth phase tunability range of more than 360°, it is not necessary to employ the slightly lossier resonance of the r = 67 μm configuration in the final design. Therefore, the DRA has a large phase tunability range, over which it exhibits loss no greater than 0.32 dB, which is highly beneficial to a reflectarray application.[46] Note, the $TE_{01\delta}$ mode of resonance can be excited only with asymmetry, which in this case is the result of the obliquely incident excitation.

Array Design. As a proof-of-concept, the DRA-based reflectarray is designed to function as an off-axis focusing mirror at 1 THz, as shown in Figure 2. The polar coordinate system in this diagram is illustrated with an arbitrary point $P = (d,\theta,\varphi)$. A collimated beam impinges on the surface of the reflectarray with an incidence angle of 45° and is focused to the point F, defined by the polar coordinates d_f = 150 mm, θ_f = 45°, and φ_f = 180°. The transformation from a collimated beam to a focused beam is achieved with the phase distribution shown in the inset of Figure 2.

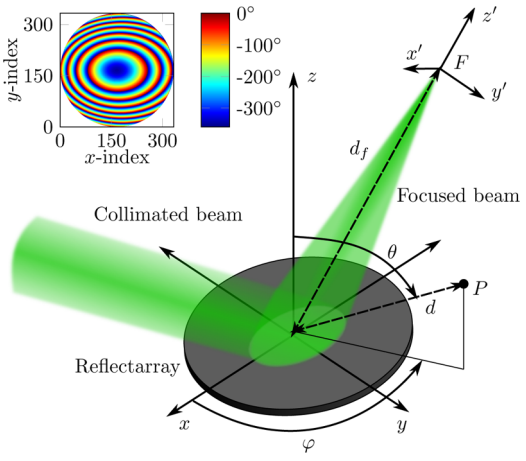

Figure 2. Expanded view of the focused terahertz reflectarray general architecture. Note the point F is the origin of a secondary coordinate system, (x',y',z'), which coincides with the focal plane of the reflectarray, and is defined in order to simplify the presentation of results. Inset shows the required phase distribution on the reflectarray surface, which is roughly 50 mm in diameter.

The focusing reflectarray design is performed using a simplified inverse process, which is valid due to reciprocity. The propagation direction is effectively reversed, and hence the focal point is replaced by a point-source virtual feed at point F that illuminates the surface, as in conventional reflectarrays. The reflectarray transforms the spherical wave radiated by the virtual feed into a collimated beam toward the direction defined by θ = 45°, φ = 0° by means of phase discontinuities introduced by the DRA elements. The phase distribution required to produce this transformation depends on the position of the feed and the propagation constant in free space and is detailed in the Methods section.[16] By convention, the phase shift has been defined as a negative value, with the higher absolute value in the center of the reflectarray.

Note the phase distribution is necessarily inhomogeneous, which results in neighboring elements of different sizes. There are two concerns that arise from this fact. First, this is inconsistent with the fact that the modeling of the individual elements employs Floquet ports that assume periodicity, and hence homogeneity. However, the variation in cylinder radius is sufficiently gradual that local periodicity can be assumed, and hence any alteration in response that results from the inhomogeneity can be neglected. Second, the nonuniform arrangement breaks resonator symmetry. In the case of normal incidence, this would result in the excitation of asymmetric modes, which would alter the response. However, oblique excitation is employed, which is asymmetric by nature, and hence these modes are accounted for. Therefore, the asymmetry that results from resonator inhomogeneity will not have a significant impact, which is an advantage of employing oblique excitation in such a reflectarray design.

Fabrication. In order to realize the required phase distribution, the phase response is controlled locally by careful selection of cylinder radius, as per the parametric analysis presented in Figure 1f,g. This parametric analysis is used to map the required phase distribution to the required radius, with results shown in Figure 3a. An automated procedure is employed to lay out this aperiodic arrangement into a mask for fabrication.

This device is fabricated using a process involving SU-8 assisted bonding, photolithography, and plasma-enhanced deep reactive ion etching. Micrographs of the fabricated device, showing silicon cylinders on a gold thin film, are given in Figure 3b,c, and the nonuniformity required to peform beam manipulation is clearly visible. These images show clearly defined, high-quality silicon cylinders, with sharp edges. This attests to the efficacy of the fabrication procedure utilized to realize these microstructures.

Characterization of Focal Spot. The reflectarray is employed to focus a collimated beam, and the focal point is characterized using terahertz time-domain spectroscopy (THz-TDS) in order to validate its performance. Results at the operating frequency of 1 THz are given in Figure 4. The measured magnitude profile in Figure 4a clearly shows a well-defined focal spot. Additionally, the measured phase profile is shown in Figure 4d, and it can be seen that phase is

DOI: 10.1021/acsphotonics.6b00102
ACS Photonics 2016, 3, 1019−1026

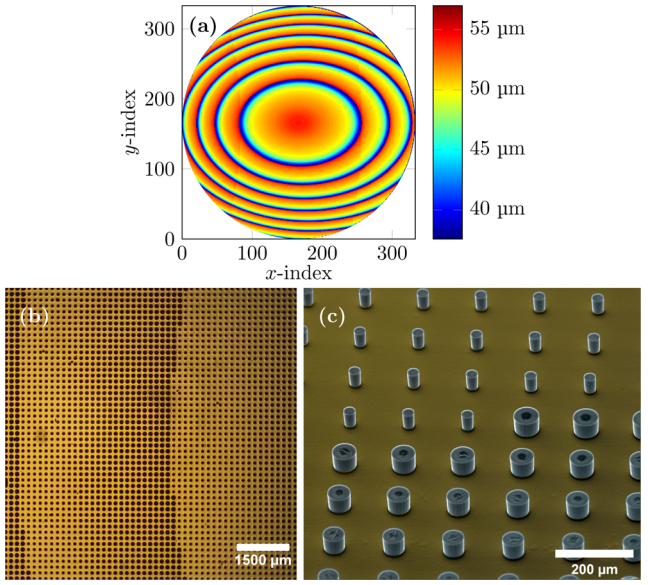

Figure 3. Realized reflectarray structure: (a) required cylinder radii, (b) optical microscope image, and (c) false-color scanning electron micrograph.

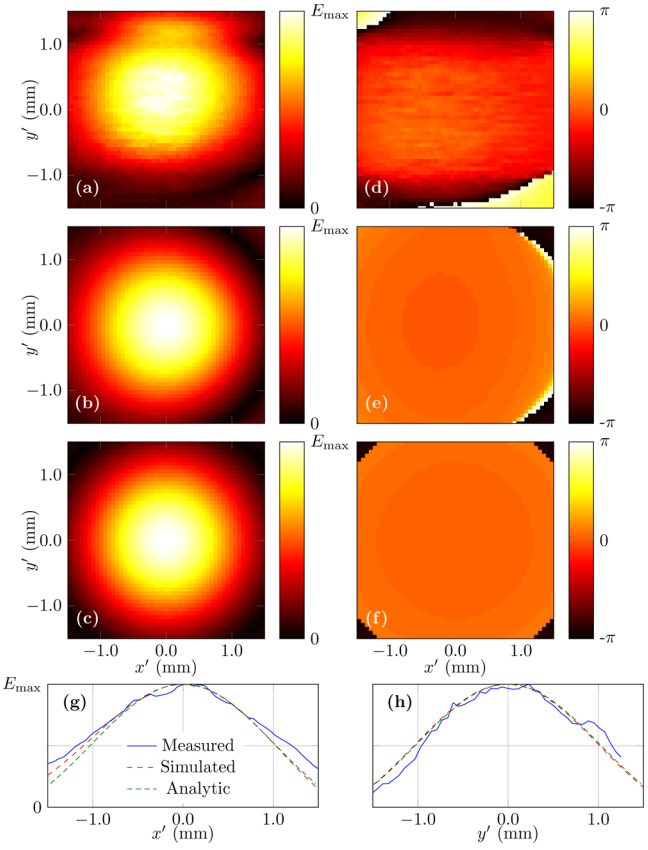

Figure 4. Beam profile of the focal spot at 1 THz. (a) Measured field magnitude distribution, (b) simulated field distribution, (c) analytically predicted field distribution,[47] (d, e, f) corresponding phase profiles for a−c, respectively, and (g, h) cross-sectional linear field distribution amplitudes. Note the measured profile in h is offset to coincide with the other plots. All plots are in linear scale.

approximately constant over the area of the focal spot, as expected for a focused beam.

In order to confirm that the measured spot is in agreement with expectation, a numerical simulation involving the Huygens−Fresnel principle[48] is employed, and results are shown in Figure 4b,e. Details of this simulation are provided in the Methods section. The simulated field profile is consistent with measured results, as there is a focal spot of comparable size in the magnitude plot, and the phase response is approximately constant. Additionally, the finite-size focusing mirror reflectarray can be treated abstractly as the focusing of a Gaussian beam that is truncated to a certain radius, for which an analytical solution exists.[47] This analytical model is employed as a secondary means to predict the field distribution of the focal spot, as shown in Figure 4c,f. In order to compare the measured, simulated, and analytically predicted focal spot in detail, cross-sectional field amplitude distributions are given in Figure 4g,h. It can be seen that they are all in strong agreement. Note that there is a slight discrepancy between the simulated and analytic results shown in Figure 4g for negative values of x'. This is a consequence of the oblique excitation, which introduces a small degree of asymmetry. This is accounted for in the numerical modeling, but the analytical model is only strictly valid for device-normal propagation.

A smaller focal spot size may be desirable for various applications, such as high-resolution imaging. It is therefore worth noting that the size of the focal spot is approximately proportional to focal length,[49] and hence it is possible to reduce focal spot size by reducing the focal length of the reflectarray. This is achieved by adjusting the phase distribution accordingly, as expounded in the Methods section. There are, however, practical limitations to this approach, as a shorter focal length will introduce larger deviations from the nominal incidence angle of 45°, which invokes undesirable modes and blind spots. Additionally, due to the diffraction limit, the minimum diameter of a focused beam is approximately equal to a wavelength.

Broadband Performance. Given that THz-TDS is employed to characterize the DRA reflectarray, it is possible to evaluate the field profile at frequencies other than the operating frequency of 1 THz. As such, the focal spots at frequencies within a 20% bandwidth are given in Figure 5. Both linear magnitude and phase are given for each focal spot. The results show that a focal spot is maintained over a frequency range of at least 200 GHz, from 0.9 to 1.10 THz. From the corresponding phase profiles in this frequency range given in Figures 5f−j, it is clear that, as with the results at 1 THz, the phase profile is approximately constant in the vicinity of the focal spot.

From comparison between Figure 5c and e, the focal spot at 1.1 THz is slightly smaller than that at 1.0 THz. This is likely due to the fact that the beam waist of a focused Gaussian beam is roughly proportional to wavelength.[49] Additionally, it is possible that the distance between the reflectarray center and the plane of measurement is slightly too great, leading to a system that is better aligned for a slightly higher frequency. This is due to the fact that the focal length of flat lenses typically increases with frequency, as the phase gradient of a flat lens scales linearly with wavelength.

Efficiency. Of key interest to the performance of this device is the efficiency, and hence further measurements are taken in order to determine the overall efficiency of the reflectarray. Details of these measurements are given in the Methods section. The results are presented in Figure 6, and it can be seen from these results that, within experimental tolerances, the

DOI: 10.1021/acsphotonics.6b00102
ACS Photonics 2016, 3, 1019−1026

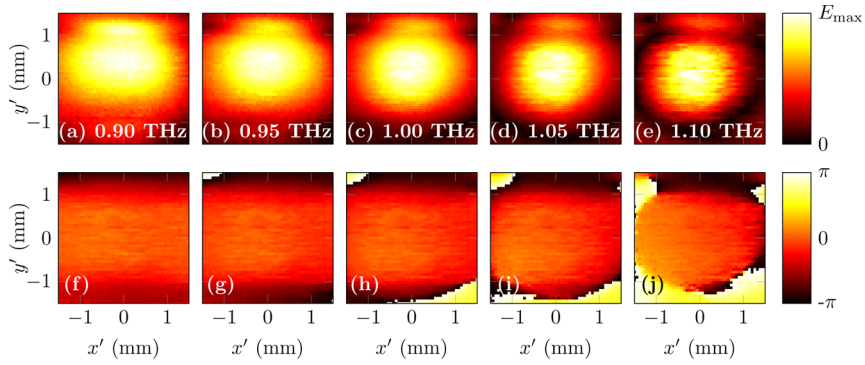

Figure 5. Broadband performance of DRA reflectarray. (a–d) Linear magnitude distribution of focal spot from 0.90 to 1.10 THz and (e–h) phase distribution of focal spot from 0.90 to 1.10 THz.

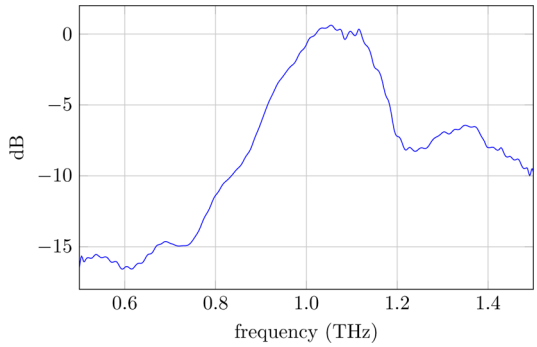

Figure 6. Efficiency of DRA reflectarray in comparison to reflection from an unpatterned gold mirror.

device has negligible loss. This is evidence of the high efficiency of the intrinsic silicon DRAs. Furthermore, from this measurement we extract a 3 dB bandwidth of 18%. It is also worth noting that the operating frequency has slightly shifted from the design frequency of 1.0 THz to 1.05 THz. This is consistent with previous observations suggesting that the system may be better aligned for a maximum at a slightly higher frequency.

Antenna Gain. Given that the reflectarray is capable of focusing a collimated beam to a fine point, by the principle of beam reciprocity, the same device is also cabable of collimating a divergent beam. Both modes of operation can be utilized in order to provide a high-gain antenna; when collimating, it operates as a transmitter, and when focusing, it operates as a receiver. With the aim of evaluating antenna gain, the far-field radiation patterns in gain are computed, using an analytical technique that is described in the Methods section. Analytical methods have been chosen to determine antenna gain for ideal illumination, due to practical constraints concerning experimental evaluation of radiation pattern. This technique makes use of an ideal feed, with near-uniform illumination of the reflectarray. The evaluated radiation patterns are presented in Figure 7. The maximum gain computed for these ideal illumination conditions is 48.5 dB, which demonstrates the capability of the reflectarray to provide high antenna gain, and hence its suitability for terahertz communications applications.

CONCLUSION

A DRA-based terahertz reflectarray is shown to have negligible loss. As proof of concept, this particular device is designed to operate as an off-axis focusing mirror. Measurements reveal a focal spot that conforms to expectation and a 3 dB bandwidth of 18%. This demonstration of a highly efficient DRA-based reflectarray opens opportunities for more advanced devices in the terahertz range, such as holograms and anisotropic devices for beam-forming and polarization control applications. Such efficient and versatile devices are expected to make a significant impact across broad fields of terahertz technology. Terahertz communications in particular will benefit from the ability to increase antenna gain and customize radiation patterns, with negligible loss.

METHODS

Numerical Modeling of the Terahertz DRA. The DRAs are modeled using the commercially available software package CST Microwave Studio. Floquet boundary conditions are employed to model a 2D array of homogeneous elements that is of infinite extent. In the case of normal incidence, this would result in total resonator symmetry, which would suppress any

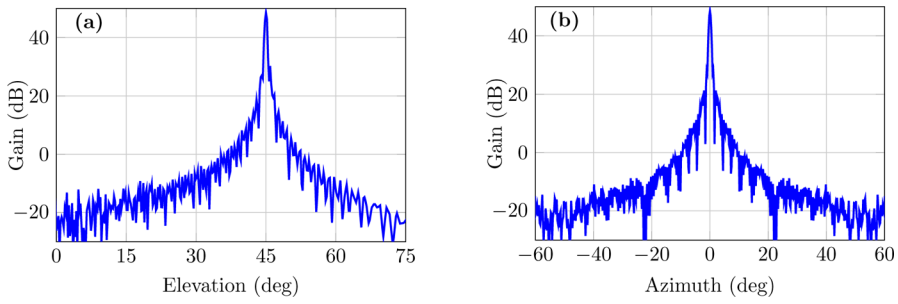

Figure 7. Far-field radiation patterns in gain for the designed reflectarray antenna working as collimator. (a) Elevation plane. (b) Azimuth plane, with an elevation angle of 45°.

DOI: 10.1021/acsphotonics.6b00102
ACS Photonics 2016, 3, 1019–1026

modes requiring asymmetry. However, oblique incidence at 45° is employed in the present work, which breaks resonator symmetry for a homogeneous array, and hence asymmetric modes are accounted for. Additionally, the nonuniformity of the reflectarray would result in breaking resonator symmetry, which can significantly alter response.[50] However, the difference in radius between an element and its immediate neighbors is usually small, and hence local homogeneity can safely be assumed to be an acceptable approximation. The only large difference between neighboring radii occurs at phase wrap-around, which occupies a negligible portion of the array area.

Drude models are utilized for both gold and silicon in order to account for realistic losses. For the silicon, the manufacturer provides a minimum resistivity of 2 kΩ, from which a carrier concentration of 2×10^{12} cm^{-3} and a mobility of 1360 cm^2 V^{-1} s^{-1} are determined,[51] in order to implement the Drude model. For the gold thin film, given the low skin depth in this frequency range, a surface impedance model is adequate.[39] A dc conductivity of 4.1×10^7 S m^{-1} and scattering relaxation time of 0.15 ps[52,53] are employed to evaluate the Drude model of gold.

Required Phase Distribution. The phase-shift, ϕ_i, that is introduced by each element of the reflectarray to convert a spherical wave from a point-source feed into a collimated beam toward a given spatial direction (θ,φ) in the far-field is computed using the following equation:[16]

$$\phi(x_i, y_i) = k_0(d_i - (x_i \cos\varphi + y_i \sin\varphi)\sin\theta) \quad (1)$$

where k_0 is the propagation constant in free-space, $(x_i, y_i, 0)$ are the Cartesian coordinates of the element i, and d_i is the distance from the phase center of the feed to the center of each element of the reflectarray, which is given by

$$d_i = \sqrt{(x_F - x_i)^2 + (y_F - y_i)^2 + (z_F - z_i)^2}$$

. Note that, in the designed reflectarray, $d_i = d_F = 150$ mm only at the center of the reflectarray. In the present design, the point F is defined by $(x_F, y_F, z_F) = (-106.066, 0, 106.066)$ mm. The resulting phase distribution is given in the inset of Figure 2.

Radius Adjustment of Dielectric Resonators. During the array design procedure, a divergent beam impinges on the surface of the reflectarray, and hence the incident rays are not parallel. Although the variation of the angle of incidence from the feed point, F, to the center of each reflectarray element is small, it is taken into consideration for an accurate design. Figure 8a and b show respectively the angles of incidence θ_{inc} and φ_{inc} at each element of the array. Both angles have been discretized to the closer value $\theta_{inc} = 39.75°$, 45.00°, or 50.25° and $\varphi_{inc} = -9°$, 0°, or 9° before being used in the design of the reflectarray. For all nine angles of incidence considered, a separate parametric sweep is performed, and the results are utilized to inform the selection of cylinder radius.

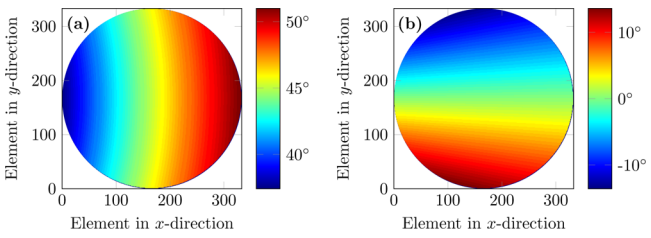

Figure 8. Angles of incidence from the feed point onto each element of the reflectarrays: (a) θ_{inc} and (b) φ_{inc}.

Mask Layout. In order to facilitate handling and compensate misalignments during experimental evaluation, the reflectarray has been designed using a circular surface with an oversized diameter of 49.95 mm, which equates to a row of 333 elements across the diameter. The resulting structure has more than 87 000 elements, in an aperiodic arrangement. In order to realize the photolithography mask required for this relatively complicated layout, an automated procedure is required. This automation is realized via a python script, which interfaces the data output from the simulation results with the IPKISS mask creation software[54] to output a GDSII design file that is compatible with commercial mask foundries.

Fabrication. An unconventional microfabrication process is employed for the realization of the single-crystal silicon-on-metal microstructure. This fabrication procedure is very precise and has tolerances in the order of ±1 μm for resonator diameter, which is well below the diameter values employed, ranging between 75 and 114 μm. First, a gold thin film with a thickness of 200 nm, which is greater than skin depth in this frequency range, is deposited onto a supporting silicon wafer. A 0.5 μm thick SU-8 layer is then spin-coated onto the metal film, and a 125 μm intrinsic silicon wafer is bonded to the substrate by lamination. Note that, while SU-8 is a lossy dielectric in the terahertz range,[55,56] the layer is used as an adhesive and is sufficiently electrically thin that it can be neglected in simulations. Finally, the silicon layer is thinned and patterned using a combination of deep reactive ion etching and photolithography, to realize the required arrangement of silicon cylinders on a gold ground plane. The details of this fabrication process were described in our previous work.[44]

Experimental Characterization of Focal Spot. Characterization of the focal spot is performed using the experimental setup shown in Figure 9. A fiber-coupled THz-TDS system is employed, which allows the receiver to move freely and facilitates raster-scanning. The sample is set at a 45° angle with respect to the transmitter and receiver and is excited by a collimated beam with TE polarization. The collimated beam is best approximated by a Gaussian beam, but in practice the beam cannot be of infinite extent in the $x'y'$-plane; hence it is truncated to a certain radius. In this case, both the beam width radius and the truncation radius are 17 mm. The receiver is raster-scanned in the $x'y'$-plane at point F in order to determine the field profile of the focal spot. The scanning resolution is 60

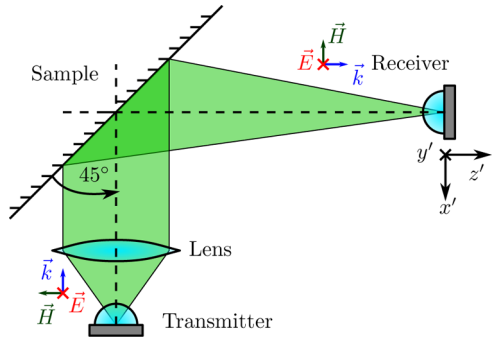

Figure 9. Measurement setup, using TE-polarized fiber-coupled photoconductive antennas. The reflective sample is set at a 45° angle, and the detector is raster-scanned in the focal plane.

DOI: 10.1021/acsphotonics.6b00102
ACS Photonics 2016, 3, 1019−1026

μm, which is equal to $\lambda/5$ at the operating frequency. An area of 3.06×3.06 mm^2 is scanned, with a total measurement time of ~20 h, and the results are shown in Figure 4a,d.

Experimental Characterization of Efficiency. In order to evaluate the efficiency of the reflectarray, a single-pixel measurement is taken at the maximum of the field profile in the focal plane. Then the focusing mirror sample is replaced with a flat gold mirror, and a polymethylpentene lens with a 50 mm focal length is placed in the path of the beam. As a reference, a measurement is taken at the maximum of the focal plane of the lens. The measurement of the focusing mirror is normalized against the reference, taking into account the absorption and reflection losses due to polymethylpentene.[57] Note that, in both cases, the acceptance angle of the receiver is such that the majority of the energy is collected.

Numerical Modeling of Focusing Reflectarray. The following procedure is employed to model the focusing operation of the reflectarray and generate the results shown in Figure 4b,e. The reflection field profile at the surface of the reflectarray is determined element-wise and is imposed upon an incident beam. The magnitude and phase response of each element is provided by the parametric analysis given in Figure 1f,g, and a 2D Gaussian function, truncated to a 17 mm radius, is employed to simulate the collimated beam excitation. To account for oblique excitation, the lattice constant in the x-dimension is scaled by a factor of $\cos(\pi/4)$. Finally, the Huygens–Fresnel principle is employed to forward-propagate the field profile by the focal length of 150 mm.

Calculation of Antenna Gain. The gain of the reflectarray is computed using the method described by Huang and Encinar[16] and demonstrated extensively in the literature,[16,17,58−60] but assuming quasi-uniform illumination on the surface of the reflectarray. First, the field incident at each element is calculated by modeling the radiation pattern of the feed as a $\cos^q \theta$ function. From the incident field and the scattering parameters of each element, the reflected field is calculated in Cartesian coordinates for the corresponding polarization. Then, from the tangential component of the reflected electric field on the surface of the reflectarray, the radiation pattarns are computed. Finally, the reflectarray gain is computed as

$$G(\theta, \phi) = \frac{|E(\theta, \phi)|^2 4\pi r^2}{2\eta_0 P} \quad (2)$$

where $\eta_0 = 376.7\ \Omega$ is the intrinsic impedance of free space and P is the total power radiated by the feed. With the aim of having a uniform illumination on the surface of the array, only impacted by the path length, $q = 1$ has been chosen to describe the feed. This results in less than 2 dB difference between the maximum and minimum illumination, while neglecting spillover losses.

AUTHOR INFORMATION

Corresponding Author

*E-mail: daniel.headland@adelaide.edu.au.

Notes

The authors declare no competing financial interest.

ACKNOWLEDGMENTS

This work is dedicated to Julien Perruisseau-Carrier, who jointly conceived the idea and passed away on June 6, 2014. D.A. and C.F. acknowledge the Australian Research Council Future Fellowship funding scheme under FT120100351 and FT100100585, respectively. This work was partially supported by the European Union (Marie Curie IEF 300934 RASTREO project) and the Swiss National Science Foundation (Project 133583).

REFERENCES

(1) Song, H.-J.; Nagatsuma, T. Present and future of terahertz communications. *IEEE Trans. Terahertz Sci. Technol.* **2011**, *1*, 256–263.

(2) Kleine-Ostmann, T.; Nagatsuma, T. A review on terahertz communications research. *J. Infrared, Millimeter, Terahertz Waves* **2011**, *32*, 143–171.

(3) Reid, C. B.; Pickwell-MacPherson, E.; Laufer, J. G.; Gibson, A. P.; Hebden, J. C.; Wallace, V. P. Accuracy and resolution of THz reflection spectroscopy for medical imaging. *Phys. Med. Biol.* **2010**, *55*, 4825.

(4) Yu, C.; Fan, S.; Sun, Y.; Pickwell-MacPherson, E. The potential of terahertz imaging for cancer diagnosis: A review of investigations to date. *Quant. Imaging Med. Surg.* **2012**, *2*, 33–45.

(5) Luukanen, A.; Appleby, R.; Kemp, M.; Salmon, N. *Terahertz Spectroscopy and Imaging*; Springer, 2013; pp 491–520.

(6) Zeitler, J. A.; Taday, P. F.; Newnham, D. A.; Pepper, M.; Gordon, K. C.; Rades, T. Terahertz pulsed spectroscopy and imaging in the pharmaceutical setting—a review. *J. Pharm. Pharmacol.* **2007**, *59*, 209–223.

(7) Shen, Y.-C. Terahertz pulsed spectroscopy and imaging for pharmaceutical applications: A review. *Int. J. Pharm.* **2011**, *417*, 48–60.

(8) Koch, M. *Terahertz Frequency Detection and Identification of Materials and Objects*; Springer, 2007; pp 325–338.

(9) Federici, J.; Moeller, L. Review of terahertz and subterahertz wireless communications. *J. Appl. Phys.* **2010**, *107*, 111101.

(10) Schneider, T.; Wiatrek, A.; Preußler, S.; Grigat, M.; Braun, R.-P. Link budget analysis for terahertz fixed wireless links. *IEEE Trans. Terahertz Sci. Technol.* **2012**, *2*, 250–256.

(11) Schneider, T. Ultrahigh-bitrate wireless data communications via THz-links; possibilities and challenges. *J. Infrared, Millimeter, Terahertz Waves* **2015**, *36*, 159–179.

(12) Wichmann, M.; Scherger, B.; Schumann, S.; Lippert, S.; Scheller, M.; Busch, S. F.; Jansen, C.; Koch, M. Terahertz Brewster lenses. *Opt. Express* **2011**, *19*, 25151–25160.

(13) Scherger, B.; Jördens, C.; Koch, M. Variable-focus terahertz lens. *Opt. Express* **2011**, *19*, 4528–4535.

(14) Scherger, B.; Scheller, M.; Jansen, C.; Koch, M.; Wiesauer, K. Terahertz lenses made by compression molding of micropowders. *Appl. Opt.* **2011**, *50*, 2256–2262.

(15) Han, D.; Lee, K.; Lim, J.; Hong, S. S.; Kim, Y. K.; Ahn, J. Terahertz lens made out of natural stone. *Appl. Opt.* **2013**, *52*, 8670–8675.

(16) Huang, J.; Encinar, J. A. *Reflectarray Antennas*; John Wiley and Sons, 2008.

(17) Carrasco, E.; Barba, M.; Encinar, J. A.; Arrebola, M.; Rossi, F.; Freni, A. Design, manufacture and test of a low-cost shaped-beam reflectarray using a single layer of varying-sized printed dipoles. *IEEE Trans. Antennas Propag.* **2013**, *61*, 3077–3085.

(18) Carrasco, E.; Tamagnone, M.; Mosig, J. R.; Low, T.; Perruisseau-Carrier, J. Gate-controlled mid-infrared light bending with aperiodic graphene nanoribbons array. *Nanotechnology* **2015**, *26*, 134002.

(19) Niu, T.; Withayachumnankul, W.; Ung, B. S.-Y.; Menekse, H.; Bhaskaran, M.; Sriram, S.; Fumeaux, C. Experimental demonstration of reflectarray antennas at terahertz frequencies. *Opt. Express* **2013**, *21*, 2875–2889.

(20) Tamminen, A.; Ala-Laurinaho, J.; Mäkelä, S.; Gomes-Martins, D.; Häkli, J.; Koivisto, P.; Rantakari, P.; Säily, J.; Tuovinen, R.; Luukanen, A. R.; Sipilä, M.; Räisänen, A. V. Near-field measurements of submillimeter-wave reflectarrays. SPIE Defense, Security, and Sensing. 2013; art. no. 871506.

DOI: 10.1021/acsphotonics.6b00102
ACS Photonics 2016, 3, 1019–1026

(21) Niu, T.; Withayachumnankul, W.; Upadhyay, A.; Gutruf, P.; Abbott, D.; Bhaskaran, M.; Sriram, S.; Fumeaux, C. Terahertz reflectarray as a polarizing beam splitter. *Opt. Express* **2014**, *22*, 16148−16160.
(22) Niu, T.; Upadhyay, A.; Withayachumnankul, W.; Headland, D.; Abbott, D.; Bhaskaran, M.; Sriram, S.; Fumeaux, C. Polarization-dependent thin-film wire-grid reflectarray for terahertz waves. *Appl. Phys. Lett.* **2015**, *107*, 031111.
(23) Cheng, Y. Z.; Withayachumnankul, W.; Upadhyay, A.; Headland, D.; Nie, Y.; Gong, R. Z.; Bhaskaran, M.; Sriram, S.; Abbott, D. Ultrabroadband reflective polarization convertor for terahertz waves. *Appl. Phys. Lett.* **2014**, *105*, 181111.
(24) Wang, D.; Gu, Y.; Gong, Y.; Qiu, C.-W.; Hong, M. An ultrathin terahertz quarter-wave plate using planar babinet-inverted metasurface. *Opt. Express* **2015**, *23*, 11114−11122.
(25) Heyes, J. E.; Withayachumnankul, W.; Grady, N. K.; Chowdhury, D. R.; Azad, A. K.; Chen, H.-T. Hybrid metasurface for ultra-broadband terahertz modulation. *Appl. Phys. Lett.* **2014**, *105*, 181108.
(26) Wang, D.; Zhang, L.; Gu, Y.; Mehmood, M.; Gong, Y.; Srivastava, A.; Jian, L.; Venkatesan, T.; Qiu, C.-W.; Hong, M. Switchable ultrathin quarter-wave plate in Terahertz using active phase-change metasurface. *Sci. Rep.* **2015**, *5*.1502010.1038/srep15020
(27) Chen, Z.; Mohsen, R.; Gong, Y.; Chong, C. T.; Hong, M. Realization of variable three-dimensional terahertz metamaterial tubes for passive resonance tunability. *Adv. Mater.* **2012**, *24*, OP143−OP147.
(28) Withayachumnankul, W.; Lin, H.; Serita, K.; Shah, C. M.; Sriram, S.; Bhaskaran, M.; Tonouchi, M.; Fumeaux, C.; Abbott, D. Sub-diffraction thin-film sensing with planar terahertz metamaterials. *Opt. Express* **2012**, *20*, 3345−3352.
(29) Headland, D.; Thurgood, P.; Stavrevski, D.; Withayachumnankul, W.; Abbott, D.; Bhaskaran, M.; Sriram, S. Doped polymer for low-loss dielectric material in the terahertz range. *Opt. Mater. Express* **2015**, *5*, 1373−1380.
(30) Walia, S.; Shah, C. M.; Gutruf, P.; Nili, H.; Chowdhury, D. R.; Withayachumnankul, W.; Bhaskaran, M.; Sriram, S. Flexible metasurfaces and metamaterials: A review of materials and fabrication processes at micro-and nano-scales. *Appl. Phys. Rev.* **2015**, *2*, 011303.
(31) Long, S. A.; McAllister, M. W.; Shen, L. C. The resonant cylindrical dielectric cavity antenna. *IRE Trans. Antennas Propag.* **1983**, *31*, 406−412.
(32) Petosa, A.; Ittipiboon, A. Dielectric resonator antennas: A historical review and the current state of the art. *IEEE Antennas Propag. Mag.* **2010**, *52*, 91−116.
(33) Leung, K. W.; Lim, E. H.; Fang, X. S. Dielectric resonator antennas: from the basic to the aesthetic. *Proc. IEEE* **2012**, *100*, 2181−2193.
(34) Lai, Q.; Almpanis, G.; Fumeaux, C.; Benedickter, H.; Vahldieck, R. Comparison of the radiation efficiency for the dielectric resonator antenna and the microstrip antenna at Ka Band. *IEEE Trans. Antennas Propag.* **2008**, *56*, 3589−3592.
(35) Abdel Wahab, W. M.; Busuioc, D.; Safavi-Naeini, S. Low cost planar waveguide technology-based dielectric resonator antenna (DRA) for millimeter-wave applications: Analysis, design, and fabrication. *IEEE Trans. Antennas Propag.* **2010**, *58*, 2499−2507.
(36) Lai, Q.; Fumeaux, C.; Hong, W.; Vahldieck, R. 60 GHz aperture-coupled dielectric resonator antennas fed by a half-mode substrate integrated waveguide. *IEEE Trans. Antennas Propag.* **2010**, *58*, 1856−1864.
(37) Takano, K.; Yakiyama, Y.; Shibuya, K.; Izumi, K.; Miyazaki, H.; Jimba, Y.; Miyamaru, F.; Kitahara, H.; Hangyo, M. Fabrication and performance of TiO_2-ceramic-based metamaterials for terahertz frequency range. *IEEE Trans. Terahertz Sci. Technol.* **2013**, *3*, 812−819.
(38) Deng, X.-D.; Li, Y.; Liu, C.; Wu, W.; Xiong, Y.-Z. 340 GHz on-chip 3-D antenna with 10 dBi gain and 80% radiation efficiency. *IEEE Trans. Terahertz Sci. Technol.* **2015**, *5*, 619−627.
(39) Zou, L.; Withayachumnankul, W.; Shah, C.; Mitchell, A.; Klemm, M.; Bhaskaran, M.; Sriram, S.; Fumeaux, C. Efficiency and scalability of dielectric resonator antennas at optical frequencies. *IEEE Photonics J.* **2014**, *6*, 4600110.
(40) Zou, C.; Withayachumnankul, W.; Shadrivov, I. V.; Kivshar, Y. S.; Fumeaux, C. Directional excitation of surface plasmons by dielectric resonators. *Phys. Rev. B: Condens. Matter Mater. Phys.* **2015**, *91*, 085433.
(41) Jamaluddin, M. H.; Sauleau, R.; Castel, X.; Benzerga, R.; Le Coq, L.; Gillard, R.; Koleck, T. Design, fabrication and characterization of a dielectric resonator antenna reflectarray in Ka-band. *Prog. Electromag. Res. B* **2010**, *25*, 261−275.
(42) Zou, L.; Withayachumnankul, W.; Shah, C. M.; Mitchell, A.; Bhaskaran, M.; Sriram, S.; Fumeaux, C. Dielectric resonator nano-antennas at visible frequencies. *Opt. Express* **2013**, *21*, 1344−1352.
(43) Zou, L.; López-García, M.; Withayachumnankul, W.; Shah, C. M.; Mitchell, A.; Bhaskaran, M.; Sriram, S.; Oulton, R.; Klemm, M.; Fumeaux, C. Spectral and angular characteristics of dielectric resonator metasurface at optical frequencies. *Appl. Phys. Lett.* **2014**, *105*, 191109.
(44) Headland, D.; Nirantar, S.; Withayachumnankul, W.; Gutruf, P.; Abbott, D.; Bhaskaran, M.; Fumeaux, C.; Sriram, S. Terahertz magnetic mirror realized with dielectric resonator antennas. *Adv. Mater.* **2015**, *27*, 7137−7144.
(45) Zou, L.; Abbott, D.; Fumeaux, C. Omnidirectional cylindrical dielectric resonator antenna with dual polarization. *IEEE Antenn. Wireless Propag. Lett.* **2012**, *11*, 515−518.
(46) Yang, F.; Nayeri, P.; Elsherbeni, A. Z.; Ginn, J. C.; Shelton, D. J.; Boreman, G. D.; Rahmat-Samii, Y. Reflectarray design at infrared frequencies: effects and models of material loss. *IEEE Trans. Antennas Propag.* **2012**, *60*, 4202−4209.
(47) Horváth, Z. L.; Bor, Z. Focusing of truncated Gaussian beams. *Opt. Commun.* **2003**, *222*, 51−68.
(48) Goodman, J. W. *Introduction to Fourier Optics*; Roberts and Company Publishers, 2005.
(49) Saleh, B. E.; Teich, M. C. *Fundamentals of Photonics*, 2nd ed.; Wiley: New York, 2007.
(50) Singh, R.; Al-Naib, I. A.; Yang, Y.; Chowdhury, D. R.; Cao, W.; Rockstuhl, C.; Ozaki, T.; Morandotti, R.; Zhang, W. Observing metamaterial induced transparency in individual Fano resonators with broken symmetry. *Appl. Phys. Lett.* **2011**, *99*, 201107.
(51) Withayachumnankul, W.; Shah, C. M.; Fumeaux, C.; Kaltenecker, K.; Walther, M.; Fischer, B. M.; Abbott, D.; Bhaskaran, M.; Sriram, S. Terahertz localized surface plasmon resonances in coaxial microcavities. *Adv. Opt. Mater.* **2013**, *1*, 443−448.
(52) Ordal, M. A.; Bell, R. J.; Alexander, R.; Long, L.; Querry, M. Optical properties of fourteen metals in the infrared and far infrared: Al, Co, Cu, Au, Fe, Pb, Mo, Ni, Pd, Pt, Ag, Ti, V, and W. *Appl. Opt.* **1985**, *24*, 4493−4499.
(53) Lucyszyn, S. Evaluating surface impedance models for terahertz frequencies at room temperature. *Piers Online* **2007**, *3*, 554−559.
(54) Bogaerts, W.; Dumon, P.; Lambert, E.; Fiers, M.; Pathak, S.; Ribeiro, A. IPKISS: A parametric design and simulation framework for silicon photonics. Proc. 9th IEEE Int. Conf. Group IV Photonics. 2012; pp 30−32.
(55) Arscott, S.; Garet, F.; Mounaix, P.; Duvillaret, L.; Coutaz, J.-L.; Lippens, D. Terahertz time-domain spectroscopy of films fabricated from SU-8. *Electron. Lett.* **1999**, *35*, 243−244.
(56) Lucyszyn, S. Comment on "Terahertz time-domain spectroscopy of films fabricated from SU-8. *Electron. Lett.* **2001**, *37*, 1267.
(57) Podzorov, A.; Gallot, G. Low-loss polymers for terahertz applications. *Appl. Opt.* **2008**, *47*, 3254−3257.
(58) Encinar, J. A.; Zornoza, J. A. Broadband design of three-layer printed reflectarrays. *IEEE Trans. Antennas Propag.* **2003**, *51*, 1662−1664.
(59) Encinar, J. A.; Zornoza, J. A. Three-layer printed reflectarrays for contoured beam space applications. *IEEE Trans. Antennas Propag.* **2004**, *52*, 1138−1148.
(60) Carrasco, E.; Barba, M.; Encinar, J. A. X-band reflectarray antenna with switching-beam using pin diodes and gathered elements. *IEEE Trans. Antennas Propag.* **2012**, *60*, 5700−5708.

DOI: 10.1021/acsphotonics.6b00102
ACS Photonics 2016, 3, 1019−1026